

Flow Simulation of N3–X Hybrid Wing-Body Configuration

Hyounghin Kim¹

Science Applications International Corporation, Cleveland, OH 44135

and

Meng-Sing Liou²

NASA Glenn Research Center, Cleveland, OH 44135

System studies show that a N3–X hybrid wing-body aircraft with a turboelectric distributed propulsion system using a mail-slot inlet/nozzle nacelle can meet the environmental and performance goals for N+3 generation transports (three generations beyond the current air transport technology level) set by NASA’s Subsonic Fixed Wing Project. In this study, a Navier-Stokes flow simulation of N3–X on hybrid unstructured meshes was conducted, including the mail-slot propulsor. The geometry of the mail-slot propulsor was generated by a CAD (Computer-Aided Design)-free shape parameterization. A body force approach was used for a more realistic and efficient simulation of the turning and loss effects of the fan blades and the inlet-fan interactions. Flow simulation results of the N3-X demonstrates the validity of the present approach.

Nomenclature

$A(x)$	=	sectional area normal to the axial direction
B	=	number of blades in a row
BLI	=	boundary layer ingestion
CAD	=	Computer Aided Design
c	=	blade chord length
F	=	body force
$f(r)$	=	set of line segments connecting control points (see Fig. 2)
H	=	height
HWB	=	hybrid wing-body aircraft
h	=	blade-to-blade gap-staggered spacing
K	=	body force coefficient
l	=	length
M	=	Mach number
MFR	=	mass flow rate
m	=	meridional coordinate
P	=	pressure
R	=	gas constant
r	=	radius
s	=	entropy
T	=	temperature
V	=	velocity
x, θ, r	=	cylindrical coordinates
α	=	blade camber angle

¹ Aerospace Engineer, Aeropropulsion Division, 3000 Aerospace Pkwy. Mail Stop VPL–2, Senior Member AIAA.

² Senior Technologist, Aeropropulsion Division, 21000 Brookpark Rd. Mail Stop 5–11, Associate Fellow AIAA

- γ = ratio of specific heats
- ρ = density
- σ = solidity

Subscripts

- c = corrected
- h = hub of blade
- LE = leading edge
- n = direction normal to local flow in a blade-to-blade section
- p = direction parallel to local flow in a blade-to-blade section
- rel = relative to the blade
- TE = trailing edge
- t = tip of blade
- tot = total

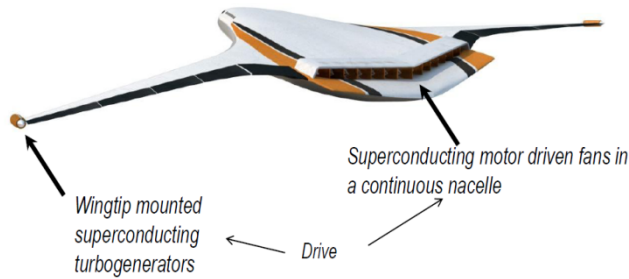
I. Introduction

The Subsonic Fixed Wing Project of the NASA Fundamental Aeronautics Program has focused on research of the next generations of civil aircraft. For the near term (N+1), midterm (N+2), and far term (N+3), specific goals have been defined for reducing noise, emissions, and fuel burn from the current state-of-the-art aviation technology.¹ To achieve our aggressive goals, especially for the N+2 and N+3 time frames, we need to explore innovative design concepts in airframes and propulsion.

The hybrid wing-body (HWB) aircraft, although not new, is an alternative design concept to the conventional tube-and-wing aircraft.² The fuselage and wings of the HWB are integrated into a flying wing, which has better aerodynamic efficiency than tube-and-wing configurations. Also, the wide airframe body of the HWB configuration is beneficial for shielding downward-propagating noise coming from the engines that are installed above the aircraft.

In comparison to conventional pylon-mounted engines, embedded engines with boundary-layer-ingestion- (BLI) offset inlets reduce ram drag, wetted area, structural weight, and noise.^{3,4} Disadvantages of the embedded engines are higher flow distortion and reduced pressure recovery at the engine faces because of the BLI-offset inlet.

The N3-X was proposed as a candidate to meet the N+3 goals.⁵ The N3-X is a 300-passenger HWB aircraft employing turboelectric distributed propulsion (TeDP), which utilizes superconducting electric generators, motors, and transmission lines (see Fig. 1(a)). The TeDP system allows power generation and thrust generation to be separated and enables a small number of turboshaft engines to drive any number of propulsors, each of which is composed of an electric motor and a fan. The N3-X was designed to have two large turboshaft engines at each wing tip to feed the engines with uniform free-stream flows. In addition, BLI propulsors are distributed in the two-dimensional mail-slot inlet/nozzle nacelle on the upper surface of the HWB near the trailing edge. A section view of an electric-motor-driven propulsor is depicted in Fig. 1(b). According to the system study in Ref. 5, the N3-X is expected to reduce mission fuel burn by more than 70 percent relative to a reference aircraft, a Boeing B777-200LR flying 7500 nm with a cruise of Mach 0.84 and a 118,100-lb payload.



(a) Overall configuration.



(b) Section view of nacelle including fan and electric motor.

Figure 1. N3–X configuration with turboelectric distributed propulsion.⁵

The conventional uniform-back-pressure boundary condition for fan faces has been used widely to simulate flow for propulsion-airframe integration problems.^{6–8} However, for integration problems with highly distorted onset flows at the fan faces, the assumption of uniform static pressure at the fan faces may not be valid. The low momentum at the low-recovery region at a fan face causes a larger local incidence angle for the fan rotor blade. This causes the fan to have a stronger suction effect, which, in turn, mitigates the flow distortion. Consequently, use of the uniform back-pressure boundary condition has produced conservative results for the flow distortion at fan faces, although it is still valid for the qualitative evaluation of inlet fan interaction problems when the diffuser flow separation does not reach to the fan face.⁹

A direct coupling of the inlet and full-annulus fan blades in the computational domain would give a more realistic simulation of the inlet-fan interaction, but the computational cost would be prohibitively large, especially for shape-design applications, in which more than tens of flow simulations are usually required. The body force approach^{9–12} has been drawing attention as an alternative to simulating the coupling with full-annulus fan blades. This approach uses body force terms to model flow turning and loss due to rotor/stator blade rows. The body force terms are added as source terms in the flow equations for grid cells swept by blade rows. Body force coefficients or parameters need to be fitted to, or interpolated from, single-passage Navier-Stokes flow simulation results or experimental test data. The body force approach allows relatively accurate flow simulation of BLI inlet-fan interaction problems that consider blade force effects without actual full-annulus simulation of the rotor/stator geometry.

In the present study, we conducted high-fidelity flow simulations of the N3–X configuration to understand the effects of the propulsion-airframe integration on the flow field and performance of the vehicle and the distributed propulsion system. A CAD-free shape parameterization was used to efficiently generate and modify the complex mail-slot nacelle geometry. A body force approach was used to incorporate the fan rotor effects of turning and flow loss.

The remainder of this paper is organized as follows. Section II presents numerical approaches for simulating flow, including the flow solver, mesh generation, and the body force method. Section III explains shape parameterization and installation approaches for the mail-slot nacelle. Section IV gives simulation results for the body force method validation as well as the flow simulation for the N3–X configuration. Finally, Section V provides the summary and conclusions.

II. Methodologies for Flow Simulation

A. Flow Solver

GO-flow,¹³ a finite-volume unstructured-grid Navier-Stokes solver, was used for the flow simulations. The compressible Reynolds-averaged Navier-Stokes equations were discretized by the cell-vertex finite volume method. Control volumes were nonoverlapping dual cells constructed around each node. Each edge connecting two nodes was associated with an area vector of the control surface, at which flow fluxes were computed. For second-order accuracy, a linear reconstruction of the primitive gas-dynamic variables inside the control volume was used in conjunction with a limiter. The inviscid flux was computed using approximate Riemann solvers, and Menter’s two-equation Shear Stress Transport (SST) model was used to incorporate turbulence effects.^{14,15} For the time integration, the Lower-Upper Symmetric Gauss Seidel (LU–SGS) implicit method was adopted.¹⁶ Parallel processing was accomplished by domain decomposition of the computational mesh and the Message-Passing Interface (MPI).

B. Body Force Model

The body force model used for this study was based on the model developed by Gong,¹¹ which makes the assumption of an infinite number of blades and axisymmetric flow in each infinitesimal blade passage. The cascade blade forces in the relative frame of reference are modeled as normal and tangential forces to the local flow, which are similar to the lift and drag forces of an airfoil.

In the present study, the formulation in Ref. 17 was used to model the normal force:

$$F_n = \frac{K_n}{h} V_n V_p + \frac{2}{c} \sin\left(\frac{\Delta\alpha}{2}\right) V_n^2 \quad (1)$$

where K_n is the normal force coefficient. Equation (1) is similar to Gong's formulation except for the second term of the right-hand side. In Eq. (1), h is the blade-to-blade gap-staggered spacing given by

$$h = \frac{2\pi r \sqrt{\sigma} \cos \alpha}{B} \quad (2)$$

where r is the radius, σ is the solidity, α is the local blade camber angle, and B is the number of blades. In Eq. (1), V_n and V_p are velocity components normal and parallel to the local cascade flow and are defined as follows:

$$V_n = V_\theta \cos \alpha - V_x \sin \alpha \quad (3)$$

$$V_p = V_x \cos \alpha - V_\theta \sin \alpha \quad (4)$$

where V_x and V_θ are velocity components in the axial and circumferential directions. In the second term on the right-hand side of Eq. (1), c is the chord length and $\Delta\alpha$ is the camber angle difference between the trailing edge TE and leading edge LE :

$$\Delta\alpha = \alpha_{TE} - \alpha_{LE} \quad (5)$$

Axial and circumferential components of the normal force are calculated by

$$F_{n,x} = F_n \frac{V_\theta}{V_{rel}} \quad (6)$$

$$F_{n,\theta} = F_n \frac{V_x}{V_{rel}} \quad (7)$$

where V_{rel} is magnitude of the blade relative velocity.

Defoe¹⁸ suggested an empirical model for determining the normal force coefficient K_n :

$$K_n = (4.2 - 3.3\alpha) \left[4.172 \left(\frac{r - r_h}{r_t - r_h} \right)^2 - 3.118 \left(\frac{r - r_h}{r_t - r_h} \right) \right] + 2.145 \quad (8)$$

where r_h and r_t are the hub and tip radius of the fan blade, respectively. The first expression in parentheses in Eq. (8), an empirically obtained term suggested in Ref. 11, is multiplied by the bracketed expression to adjust the magnitude of K_n along the spanwise direction. For this study, we adopted a formulation for K_n that is very similar to Eq. (8) but allows more flexibility:

$$K_n = (4.2 - 3.3\alpha)f(r) \quad (9)$$

where $f(r)$ is a set of line segments connecting control points with a spanwise distribution as shown in Fig. 2. The control points of $f(r)$ were adjusted to match available computational fluid dynamics (CFD) or experimental data as shown in Section IVA.

In Gong's model, components of the body force for the flow loss F_p are modeled by

$$F_p = \frac{K_p}{h} V_{rel}^2 \quad (10)$$

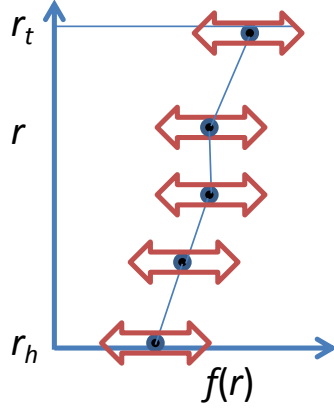


Figure 2. Definition of $f(r)$ for the body force coefficient K_p .

with $K_p = 0.05$. In Eq. (10), for a constant K_p , F_p is proportional to V_{rel}^2 , which means that the magnitude of F_p increases as the mass flow rate (MFR) increases for a fixed rotor speed. However, Chima¹⁰ showed that entropy production across a blade zone decreases as MFR increases from a near-surge to a near-choking condition, and entropy production is directly connected to F_p as

$$F_p = -T \frac{V_m}{V_{rel}} \frac{\partial s}{\partial m}, \quad (11)$$

where T is the temperature, s is the entropy, and m is the coordinate along the meridional streamline and V_m is its velocity component. For this study, we employed Eq. (11) for a better modeling of the flow loss. In Refs. 10 and 11, spanwise distributions of the entropy production across the blade region were used to determine the flow loss. We made the assumption that the entropy production is constant along the blade span and chord for a simpler modeling procedure. Thus, we could easily calculate the averaged entropy change, either from test data or CFD results for the total pressure P_{tot} and total temperature T_{tot} ratio of a blade row, by using the canonical equation of state:

$$\frac{\Delta s}{R} = \frac{\gamma}{\gamma-1} \ln \left(\frac{T_{tot2}}{T_{tot1}} \right) - \left(\frac{P_{tot2}}{P_{tot1}} \right), \quad (12)$$

where R is the gas constant, γ is the specific heat ratio, and stations 1 and 2 refer to the entrance and exit of a fan blade row, respectively. As an example, Fig. 3 shows entropy production values across a fan rotor blade row calculated by Eq. (12) with the total pressure and total temperature ratios from test data.¹⁹ In a fixed-rotor-speed line, the entropy production decreases until the minimum loss point and then increases as the MFR increases.

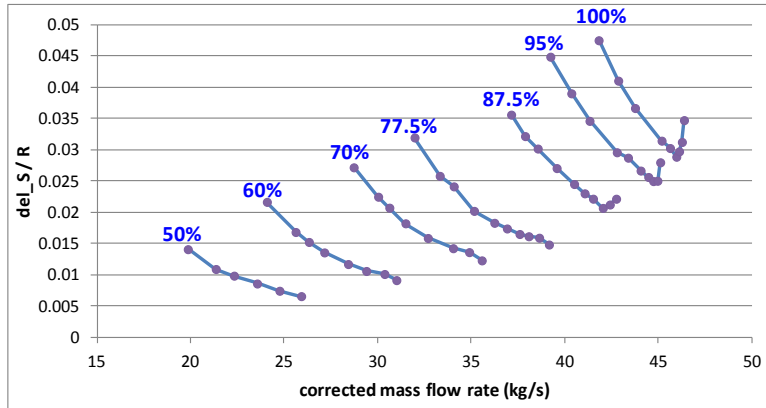


Figure 3. Mass flow rate versus entropy production of the R4 fan rotor blade row for different rotor speeds.

The entropy gradient in Eq. (11) is approximated by the entropy production of a blade row and the section chord length in the meridional plane at each radial location:

$$\frac{\partial s}{\partial m} \cong \frac{\Delta s}{x_{TE} - x_{LE}} \quad (13)$$

The three components of F_p are calculated as follows:

$$F_{p,x} = F_p \frac{V_x}{V_{rel}}, \quad F_{p,\theta} = F_p \frac{V_\theta}{V_{rel}}, \quad \text{and} \quad F_{p,r} = F_p \frac{V_r}{V_{rel}} \quad (14)$$

The averaged entropy production of a blade row changes as the MFR is varied at a constant rotor speed. The entropy production curves are fitted to quadratic or linear equations as a function of the corrected MFR. To make the actual interpolation along the polynomial functions, we need an interpolation parameter. For structured-grid approaches having axisymmetric grid sections, each grid section is treated as an independent axisymmetric flow section, and the sectional MFR is used as the interpolation parameter for cases with a distorted inflow.¹¹ In unstructured grid approaches, it is very hard to define axisymmetric sections in a three-dimensional unstructured grid. For this study, we defined the local MFR parameter as

$$MFR_c^{\text{local}} = \rho V_x A(x) \quad (15)$$

where ρ and V_x are the local density and local axial velocity, respectively, and $A(x)$ is the sectional area normal to the axial direction. The local MFR parameter becomes very small for mesh points in the boundary layer near the viscous wall where V_x is very small. To prevent non-physically large amounts of the entropy production for low and high MFR_c^{local} values, the entropy production is limited by a maximum value, which is usually set as 2.0 to 2.5 times larger than the minimum entropy production for a constant rotor speed line.

A summary of the procedure for generating the body force model follows:

- 1) Obtain an entropy production curve for a given fan geometry and rotor speed from test data or single-passage Navier-Stokes analyses as shown in Fig. 3.
- 2) Conduct least-squares fitting of the entropy production curves with linear or quadratic polynomials. If there is a minimum loss condition, as can be seen at speeds of 87.5, 95, and 100 percent in Fig. 3, divide the entropy curve into two regions by the minimum-loss MFR position, and fit the left and right regions of the curve to separate functions.
- 3) Iteratively run a three-dimensional Euler solver with the body force model to adjust the entropy curve functions to match the resulting entropy changes to the original entropy production input distribution.
- 4) Iteratively run the Euler solver with the body force model to adjust the multiplying factor to the control parameters of the function $f(r)$ in Eq. (9) to match the fan pressure ratio for the speed line. Adjust each control point separately if spanwise swirl and total pressure distributions are available and need to be matched to each other.
- 5) If the body force model will be used in Navier-Stokes simulations, run a few Navier-Stokes simulations with the body force model to quantify the effects of the hub and shroud boundary layers on the resulting entropy production. Pull down the entropy curve functions to compensate for the entropy increment in the Navier-Stokes analysis.

C. Computational Mesh Generation

An unstructured computational mesh was generated with the Mixed-Element Grid Generator in 3 Dimensions (MEGG3D) code.^{20,21} A triangular surface mesh was generated directly on a background unstructured mesh or from stereolithography (STL) data, which can be exported from a CAD model. Then, advancing front/layer methods were used to make a hybrid volume mesh. Layers of prismatic cells were generated near viscous walls, tetrahedral cells were generated in the remaining computational domain, and pyramid cells were generated between the other cells when necessary.

III. Geometry Generation of the Mail-Slot Nacelle

A. Shape Parameterization

A Fortran code was written that uses shape parameters to build mail-slot nacelles. The mail-slot nacelle shape can be divided into outer cowl and flow passages, each of which is composed of an S-duct inlet, a nozzle, a cylindrical duct connected to the inlet and nozzle, and a motor fairing center body. The S-duct, which is a transitional duct, has a sectional shape that transitions from a rectangle to a circle. The nozzle, which is also a transitional duct, has a sectional shape that transitions from a circle to a rectangle. In both the inlet and nozzle, the flow passages are separated by splitters.

The mail-slot propulsor is built up by 173 surface patches. Each surface patch has a structured plot3D data format. The neighboring patches are precisely joined without any gaps so that they share the same nodes and are “water tight” and ready for unstructured surface grid generation. Figure 4 shows some parameters for the mail-slot propulsor geometry. Other parameters such as sectional areas also are defined. Any new parameters can be readily added if necessary. The computer code can be used for parametric design and optimal shape-design studies for distributed propulsion systems with a mail-slot nacelle. Figure 5 shows a half model of a mail-slot nacelle that has 16 fans and is swept forward by 25° .

Once the water-tight nacelle surface patches are generated, the nacelle surface meshes are combined with an airframe surface mesh for a clean HWB configuration. After this installation, a computational unstructured surface mesh is generated on the combined configuration. The HWB airframe can be parameterized independently from the propulsor then combined with the propulsor to build the full N3-X configuration.

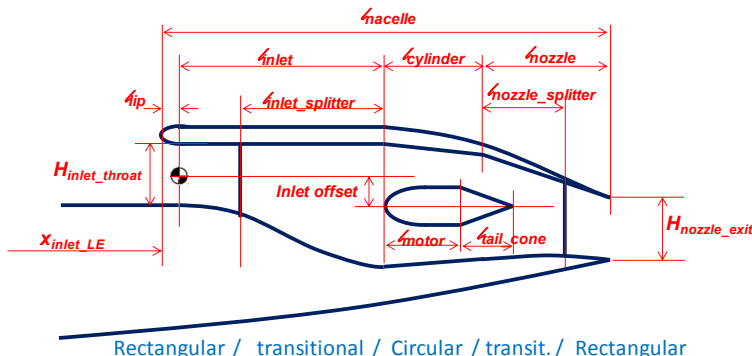


Figure 4. Side section view of schematic representation of the propulsor parameterization.

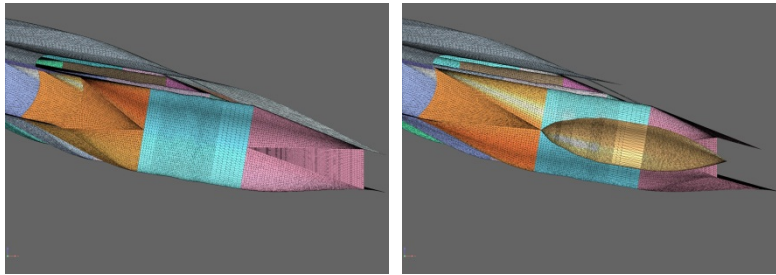
B. Installation

The steps for generating the nacelle geometry and installing it on the upper surface of an HWB configuration follow.

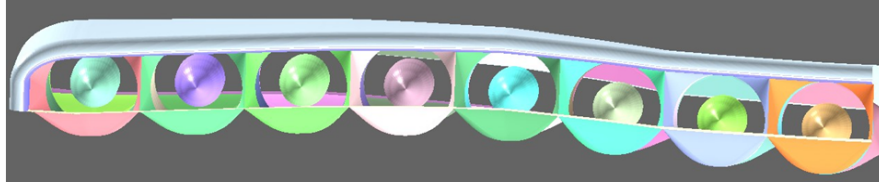
- 1) Build a nacelle geometry consistent with the airframe wing upper surface.—Since the upper surface of the wing is curved, the mail-slot propulsor geometry needs to be generated from geometric information about the upper surface of the curved wing. The propulsor and the upper surface of the wing are connected at three curves: the leading edge curve of the bottom surface of the inlet entrance, the trailing edge curve of the bottom surface of the nozzle exit, and the junction curve at the bottom of the nacelle side wall. The three curves are the left, right, and upper side curves of the top view of the nacelle shown in Fig. 5(d). Vertical coordinates were obtained for the three boundary curves of the upper surface of the wing by interpolation from the wing-surface geometry definition. At the leading and trailing edge curves, the bottom surface slopes were also defined so that the connection is C^1 continuous. The pitch angle of the cowl lip and center body of each flow passage also are set according to the local slope at the inlet entrance.

- 2) Remove the upper-surface mesh cells of the wing that are overlapped by the nacelle in the top view, Fig. 5(d).—Remove the surface cells located in the installation region to make space for the nacelle.

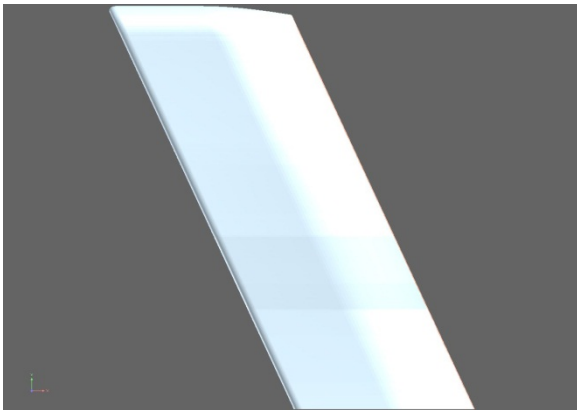
- 3) Fill the gap between the remaining upper-surface cells of the wing and the installed nacelle. In this study, we used the hole-filling function of MEGG3D.^{20,21} With the gaps filled, we are ready to generate an unstructured surface mesh. The mesh-generation methodology is presented in Section III.



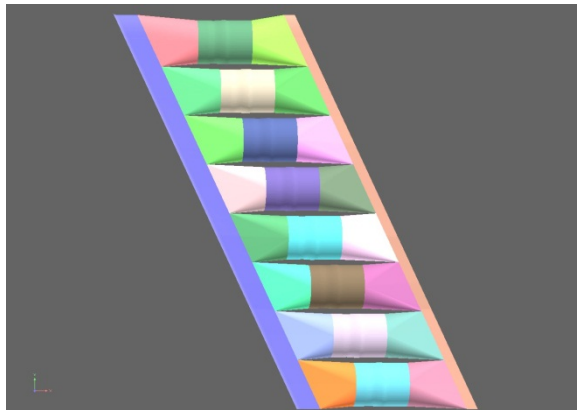
(a) Side view of transitional and cylindrical ducts. (b) Side view inside the duct and center body.



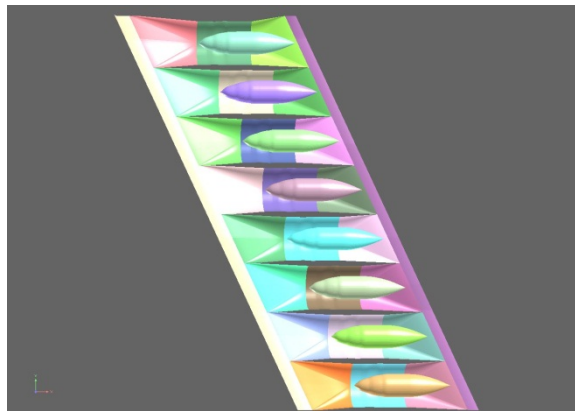
(c) Front view.



(d) Top view of nacelle surface.



(e) Inactivated outer surface of nacelle.



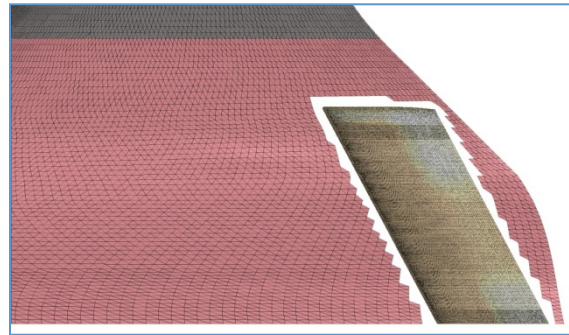
(f) Inside the flow passages.

Figure 5. Half model of a mail-slot nacelle that has 16 fans and a 25° forward sweep.

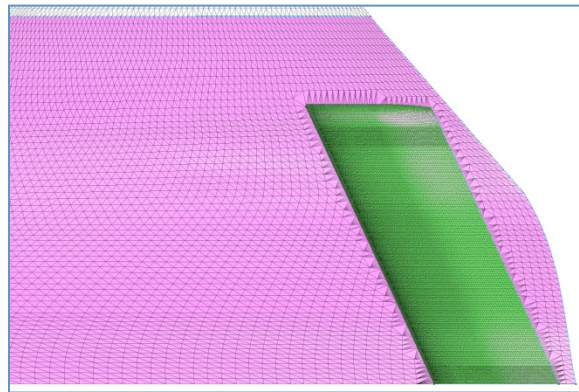
Figure 6 illustrates steps 2 and 3. The whole procedure was very efficient and did not require any time-consuming tailoring or fixing steps for the baseline geometry. Tailoring and fixing of poor quality baseline geometry is usually needed for meshing processes that are based on complex CAD geometries.

Figure 7 shows the HWB configuration with the distributed propulsion nacelle installed on the upper surface. In the present study, the installation was made so that the leading edge of the mail-slot nacelle is located at the 85% chord position at the airframe center section. The streamwise location of the nacelle also can be modified by changing the parameter x_{inlet_LE} in Fig. 4. As can be seen in Fig. 6(a), the nacelle cowl follows the spanwise variation of the wing upper surface. Also, the cowl lips are twisted down in the outboard direction according to local slopes at the inlet leading-edge on the wing surface.

After the installation procedure, the surface mesh was used as a background mesh on which a computational mesh could be generated by any unstructured mesh generator. In this study, we adopted MEGG3D for mesh generation, as mentioned in Section II. Figure 8 shows the computational mesh generated for the combined configuration. About 20 million computational mesh points are in the half model of the N3-X configuration, and the first nodes off the viscous walls are clustered to the wall so that the y^+ values at the first nodes are less than 2. At this point, the flow simulation could be conducted with the proper body force model for the fan blades.



(a) Remove the upper surface cells of the wing that are overlapped by the nacelle to make holes between the wing surface mesh and the installed nacelle. The hole size is exaggerated for clarity.



(b) Fill the holes between the upper surface mesh and the installed nacelle.

Figure 6. Nacelle installation procedure.

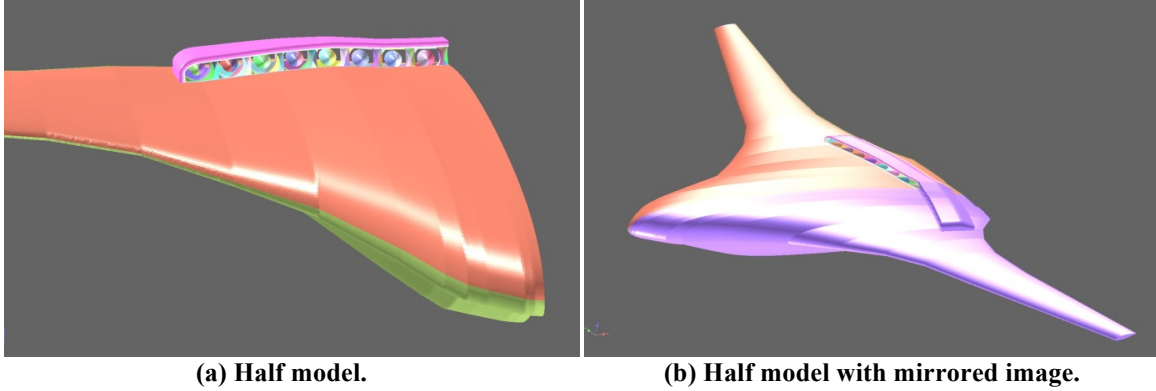


Figure 7. N3-X configuration with installed mail-slot propulsor.

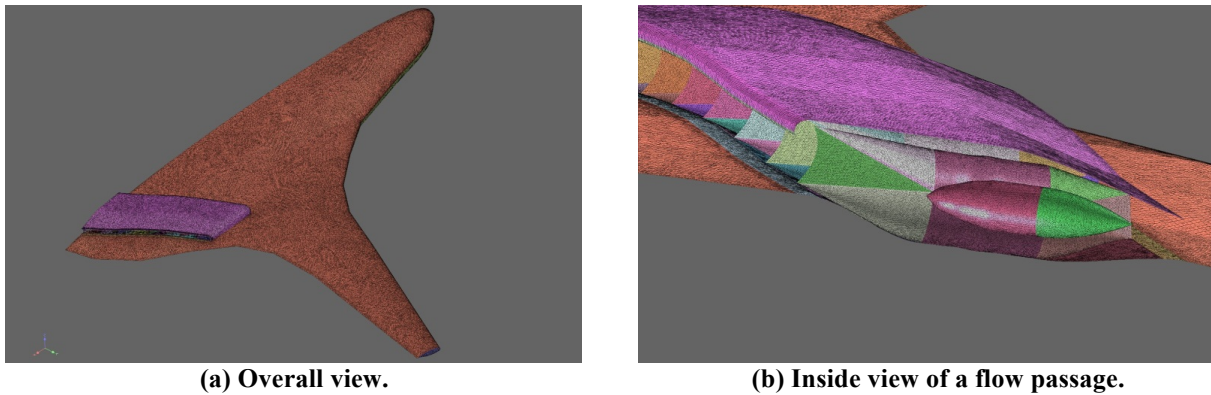


Figure 8. Computational surface mesh for N3-X.

IV. Results

A. Validation of the Body Force Model

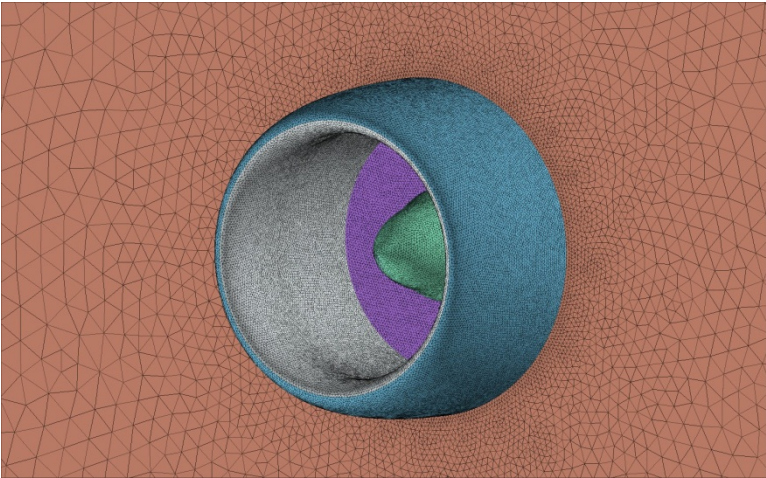
The R4 fan rotor,¹⁹ which was designed by General Electric Aircraft Engines and tested by the NASA Glenn Research Center, was selected to validate the present body force model. The R4 fan is a one-fifth scale-model representation of the bypass stage of a current-generation high-bypass turbofan engine. The fan has a 22-in. diameter and 22 wide-chord rotor blades. The stage design-point pressure ratio was 1.47 at a corrected speed of 12,657 rpm.

For single-passage Navier-Stokes flow simulations of the R4 fan, the SWIFT code²² was used. The SWIFT code is a three-dimensional, multiblock, structured-grid Navier-Stokes analysis code for turbomachinery blade rows. The code solves the Navier-Stokes equations on body-fitted grids using an explicit finite-difference scheme. The AUSM+ upwind scheme²³ was used for spatial discretization of the inviscid flux. For the thin-layer approximation, viscous terms were included in the blade-to-blade and hub-to-tip directions and were neglected in the streamwise direction. For turbulence effects, Wilcox's 2006 $k-\omega$ model with a stress limiter was selected. The discretized equations were solved with a multistage Runge-Kutta scheme with local time stepping and residual smoothing being used to accelerate convergence.

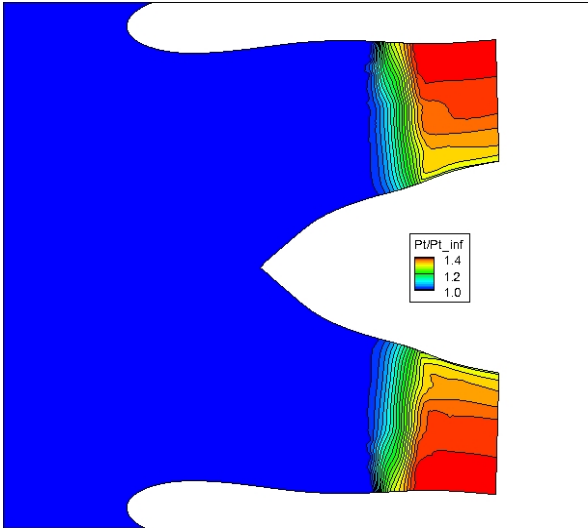
An unstructured grid with tetrahedral cells was generated around the nacelle cowling, shroud, and hub of the R4 fan test geometry, and *GO-flow* was run in an inviscid flow simulation mode with the body-force source terms added. For the fan downstream exit boundary condition, static back pressure was imposed with the radial equilibrium condition. Figure 9(a) shows the computational mesh for the clean-inflow R4 case, and Fig. 9(b) shows the total pressure contours normalized by the free-stream total pressure. The total pressure increases along the streamwise direction with an almost uniform slope.

Figure 10(a) compares the fan rotor pressure ratio versus the MFR_c at 85 percent of the design rotor speed. The test data agree very well with the results of the Swift code and the inviscid simulation with the body force model. Figure 10(b) shows that the entropy production calculated by the Euler + body force model matches the test data

well. The averaged entropy production of the R4 fan rotor decreases as the MFR increases until the peak efficiency point—approximately 42 kg/s. For MFRs higher than the peak-efficiency MFR, entropy production is proportional to the MFR because the incidence angle of the blade section deviates from the minimum loss angle.

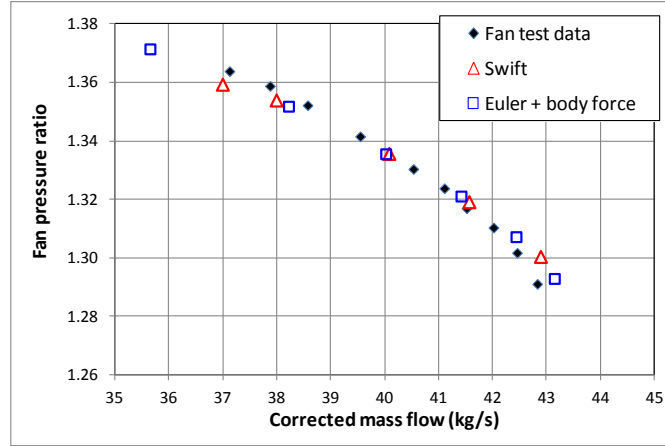


(a) Computational mesh.

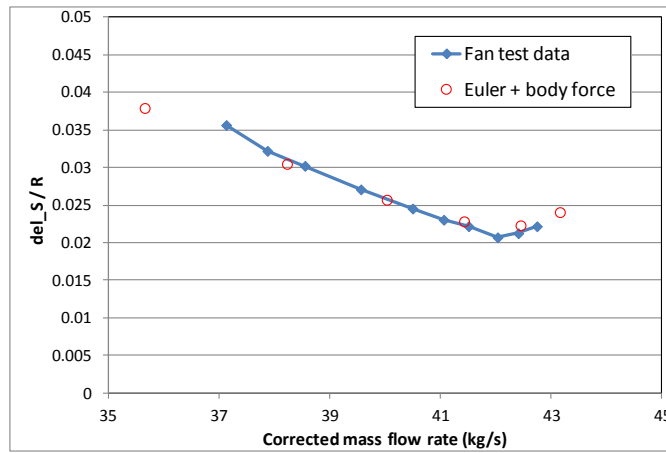


(b) Normalized total pressure contours at a center section.

Figure 9. Euler simulation of R4 fan + nacelle with body force model.



(a) Mass flow rate versus fan pressure ratio for 85-percent speed.

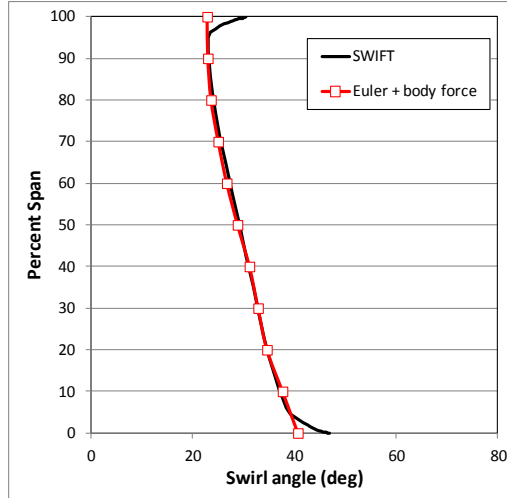


(b) Mass flow rate versus entropy production for 85-percent speed.

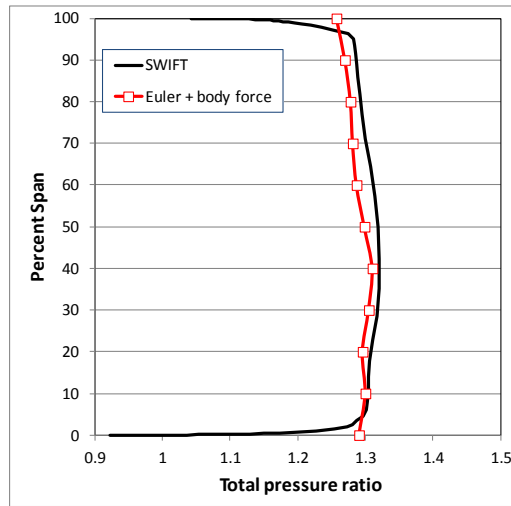
Figure 10. Comparison of body force model results with test data and the Swift code.

In Fig. 11, spanwise distributions of flow characteristics circumferentially averaged at the rotor exit plane are compared for the Swift code and the present Euler + body force model. Actually, the control points of $f(r)$ in Section IIB are adjusted to closely follow the trend of the swirl and the total pressure distributions for the flow conditions near the peak efficiency ($MFR_c = 43\text{kg/s}$). Therefore, the two results are in good agreement except near the hub and shroud walls because inviscid simulations were used with the body force approach for a fast turnaround time.

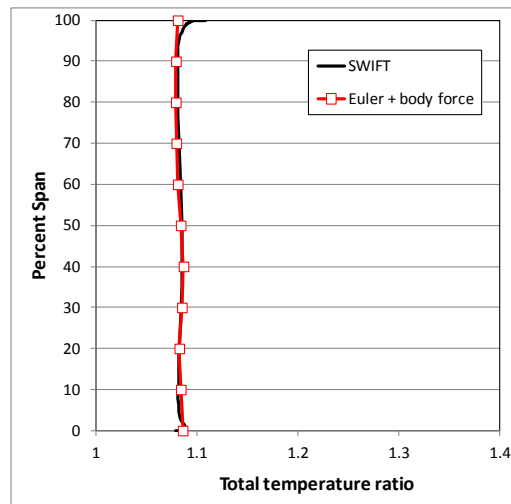
As the corrected MFR decreased to 38 kg/s, as shown in Fig. 12, deviations between the Swift code and Euler+body force results became larger, but the trend was still well captured by the body force model approach. If the control points of $f(r)$ were interpolated from two or more simulation results (instead of using constant values), the body force model approach results would be improved even further.



(a) Swirl-angle distribution.

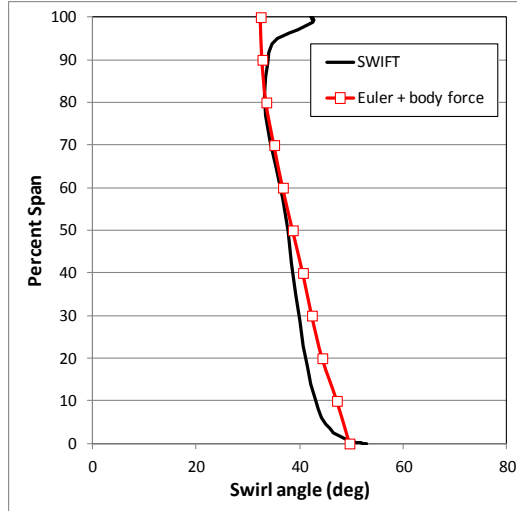


(b) Total pressure ratio distribution.

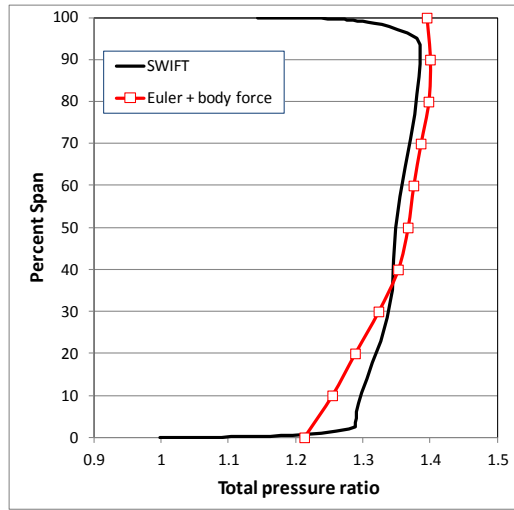


(c) Total temperature ratio distribution.

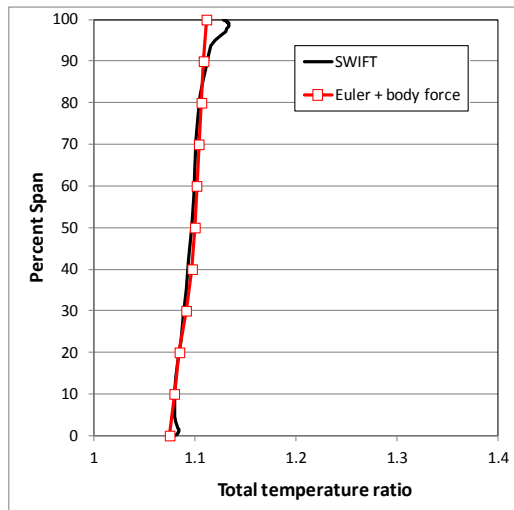
Figure 11. Comparison of rotor exit flow characteristics along the span near the choking condition ($MFR_c = 43 \text{ kg/s}$).



(a) Swirl angle distribution.



(b) Total pressure ratio distribution.



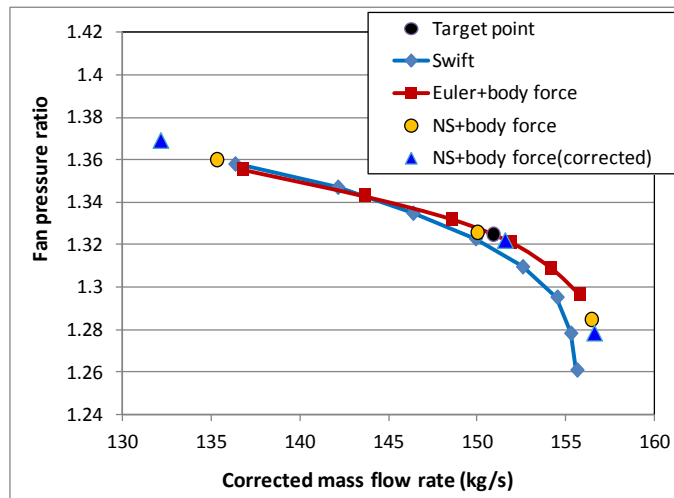
(c) Total temperature ratio distribution.

Figure 12. Comparison of rotor exit flow characteristics along the span near the surge condition ($MFR_c = 38 \text{ kg/s}$).

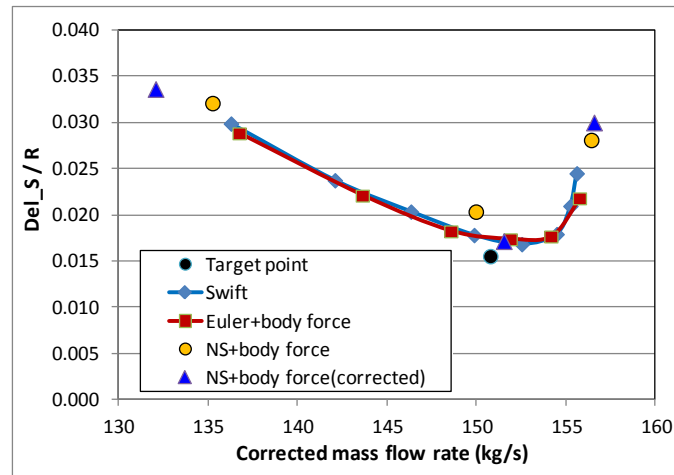
B. Flow Simulation of N3-X

The overall size and performance specifications of the propulsor fan for N3-X were interpolated from data in Table 5 of Ref. 5: fan diameter = 1.02235 m (40.25 in.), $MFR_c = 150.8$ kg/s, pressure ratio = 1.325, and rotor speed = 5329.575 rpm_c. So that a body force model could be built for an N3-X fan, the R4 fan was scaled up to have a fan diameter ratio of 40.25/22 and the blade stagger angle and rotor speed were adjusted to match the specifications. The blade stagger and rotor speed were modified, and the Swift code was run to check the modified fan's performance. Through an iterative procedure, the stagger angle was reduced by 5° and the rotor speed was determined to be 5913.667 rpm_c.

In Fig. 13, numerical results from the SWIFT code and the current Euler simulation with the body force model are well matched by the body force model buildup except near high-MFR conditions. Because the body force model will actually be applied here to a viscous flow simulation of the N3-X configuration, Navier-Stokes simulations of the modified R4 rotor with the body force model were tested. The pressure ratio does not differ significantly for the Euler and Navier-Stokes simulations, but entropy production was increased in the viscous simulation.



(a) Mass flow rate versus fan pressure ratio



(b) Mass flow rate versus entropy production.

Figure 13. Generation of the body force model for the scaled R4 fan installed on N3-X.

This is natural because the hub and shroud boundary layer effects were duplicated in the Navier-Stokes simulation and the body force model. The body force model for the Navier-Stokes simulation was, therefore, corrected by reducing entropy production by 0.003. The actual amount of entropy correction would be varied for different flow conditions and computational meshes. The triangular symbols in Fig. 13 represent the results for the

corrected body force model. There is little difference in the pressure ratio, and there is good agreement in the entropy production for the Swift code and the Euler and Navier-Stokes simulation with the body force model.

A flow simulation of the N3-X HWB configuration was conducted for a cruise flight condition: Mach 0.84, an altitude of 35,000 ft, and an angle of attack of 2° . Figures 14 and 15 shows sectional side views of local Mach number and total pressure contours for the first (passage 1) and last (passage 8) propulsor passages in the spanwise direction. The difference in the ingested boundary layer thickness can be noted from the total pressure contours. The inner passages have thicker boundary layers than the outer passages have because of the difference in distances from the airframe leading edge. Therefore, the outer passages have higher fan face recoveries and larger mass flow rates than the inner passages have. The region that is swept by the fan blade and has the body force model applied can be easily recognized as the steep axial gradient of the total pressure contours around the hub forebody. The duct and hub afterbody shapes need to be improved to reduce flow blockages and partial supersonic flows.

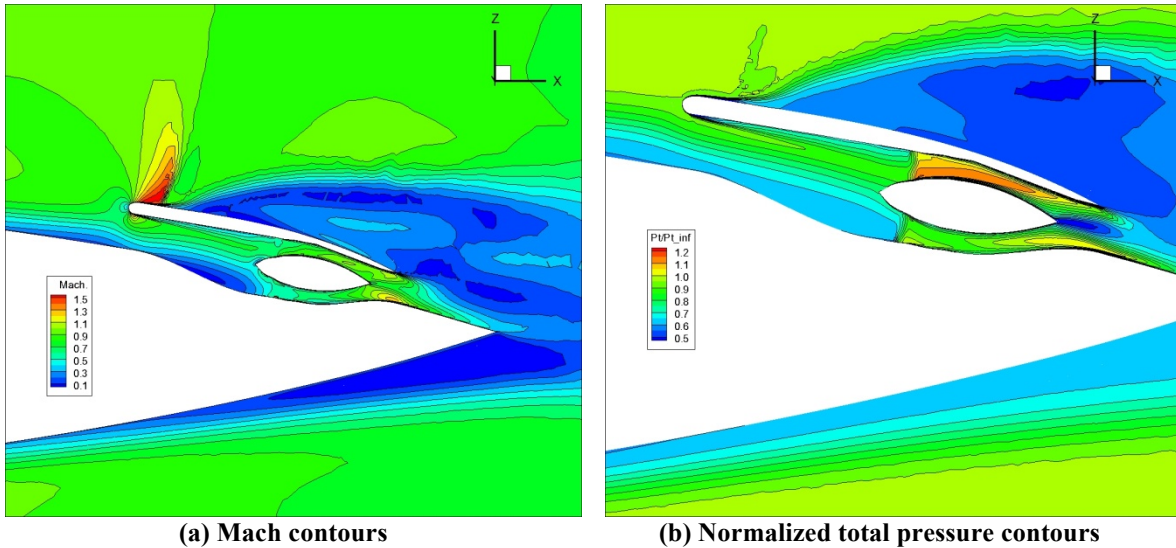


Figure 14. Center section contours for passage 1 (1st passage from the symmetric plane).

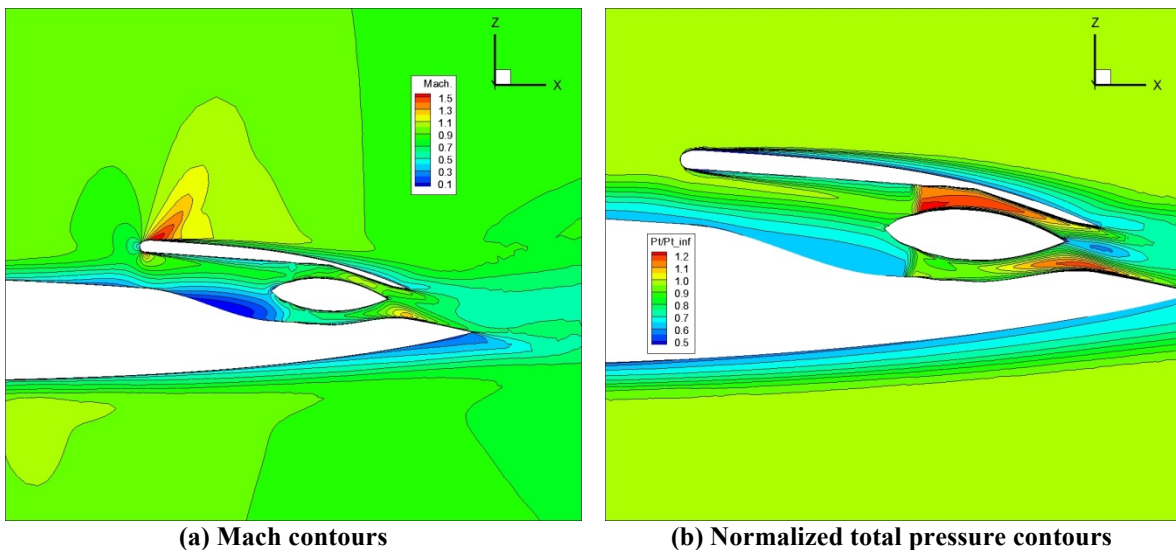


Figure 15. Center section contours for passage 8 (last passage from the symmetric plane in the spanwise direction).

As shown in Fig. 14, the first propulsor has a strong shock wave on the cowl surface and shock-induced flow separation, which need to be removed for better aerodynamic performance. Meanwhile, Fig. 15 for passage 8 shows shock-free Mach contours on the cowl surface. Figure 16 visualizes the separation bubbles with negative streamwise velocity envelopes. Small separation bubbles exist at the outboard inlet splitters, the nacelle cowl trailing edge for the vertical side wall and on the lower surface near the airframe trailing edge. The largest separation bubble occurs near the symmetric plane on the nacelle cowl surface.

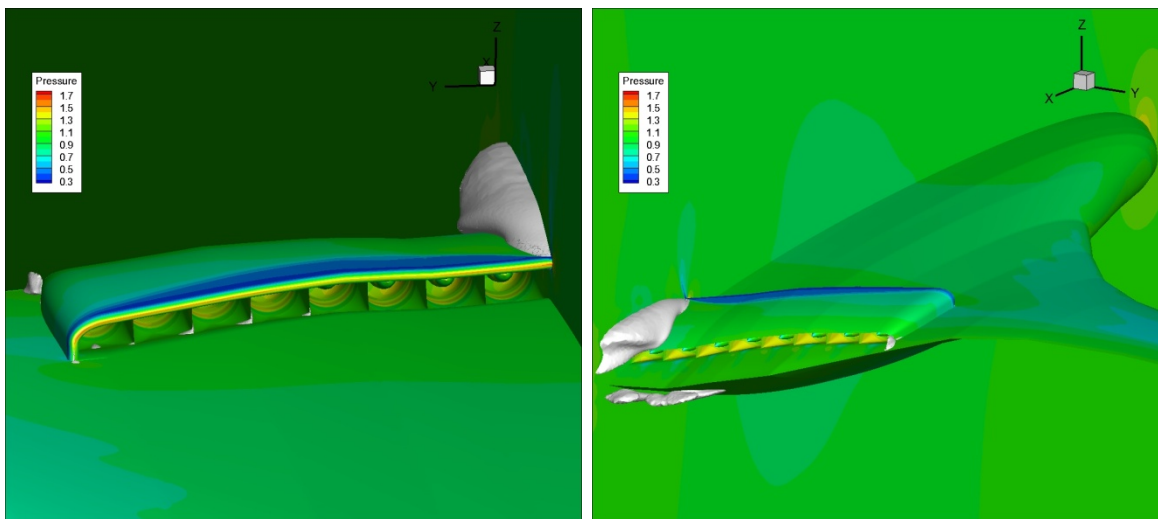


Figure 16. Surface pressure contours and visualization of separation bubbles with negative streamwise velocity isosurfaces.

V. Concluding Remarks

High-fidelity flow simulations were conducted for the N3-X hybrid wing-body configuration with the turboelectric distributed propulsion system using 16 fans in the mail-slot propulsor. The mail-slot propulsor geometry was generated by an efficient CAD (computer-aided design)-free procedure. A body force model generation procedure was suggested for efficient and accurate flow simulations of inlet-fan interaction problems. Flow simulation results for the N3-X hybrid wing-body configuration with the body force model show the validity of the present approach.

Acknowledgments

The authors are grateful for the support of the NASA's Subsonic Fixed Wing Project of the Fundamental Aeronautics Program. The N3-X clean airframe geometry was provided by Julio Chu of the NASA Langley Research Center.

References

- ¹NASA Research and Technology Program and Project Management Requirements, NASA Procedural Requirements (NPR) 7120.9. Appendix J. Technology Readiness Levels (TRLs), Feb. 5, 2008. Available at http://nodis3.gsfc.nasa.gov/displayDir.cfm?Internal_ID=N_PR_7120_0008_&page_name=AppendixJ
- ²Liebeck, R. H., "Design of the Blended Wing Body Subsonic Transport," *J. Aircraft*, Vol. 41, No. 1, 2004.
- ³Kawai, R., and Brown, D., "Acoustic Prediction Methodology and Test Validation for an Efficient Low-Noise Hybrid Wing Body Subsonic Transport," Phase I Final Report PWD08-006A, NASA Contract Number NNL07AA54C, NASA, Oct., 2008.
- ⁴Hileman, J. I., Spakovszky, Z. S., Drela, M., Sargeant, M. A., and Jones, A., "Airframe Design for Silent Fuel-Efficient Aircraft," *J. Aircraft*, Vol. 47, No. 3, 2010, pp. 956-969. See also AIAA Paper 2007-453, Jan., 2007.
- ⁵Felder, J., Kim, H. D., and Brown, G. V., "An Examination of the Effects of Boundary Layer Ingestion on Turboelectric Distributed Propulsion Systems," AIAA-2011-300, AIAA, 2011.

- ⁶Rodriguez, D. L., “Multidisciplinary Optimization Method for Designing Boundary Layer Ingestion Inlets,” *J. Aircraft*, Vol. 46, No. 3, 2009, pp. 883–894.
- ⁷Kim, H., Kumano, T., Liou, M.-S., Povinelli, L. A., and Conners, T., “Numerical Propulsion Flow Simulation of Supersonic Inlet With Bypass Annular Duct,” *J. Propul. Power*, Vol. 27, No. 1, 2011, pp. 29–39.
- ⁸O’Brien, D. M. Jr., Calvert, M. E., and Butler, S. L. “An Examination of Engine Effects on Helicopter Aeromechanics,” *AHS Specialist’s Conference on Aeromechanics*, San Francisco, CA, Jan. 23–25, 2008.
- ⁹Chima, R. V., “Rapid Calculations of Three-Dimensional Inlet/Fan Interaction,” NASA Fundamental Aeronautics 2007 Annual Meeting, New Orleans, LA, Oct. 30–Nov. 1, 2007.
- ¹⁰Chima, R. V., “A Three-Dimensional Unsteady CFD Model of Compressor Stability,” GT2006–90040, ASME, 2006.
- ¹¹Gong, Y., “A Computational Model for Rotating Stall Inception and Inlet Distortion in Multistage Compressors,” Ph.D. Dissertation, Massachusetts Institute of Technology, 1998.
- ¹²Hsiao, E., Naimi, M., Lewis, J. P., Dalbey, K., Gong, Y., and Tan, C., “Actuator Duct Model of Turbomachinery Components for Powered-Nacelle Navier-Stokes Calculations,” *J. Propul. Power*, Vol. 17, No. 4, 2001, pp. 919–927.
- ¹³Kim, H., Kumano, T., Liou, M.-S., Povinelli, L. A., and Conners, T., “Numerical Propulsion Flow Simulation of Supersonic Inlet with Bypass Annular Duct,” *J. Propul. Power*, Vol. 27, No. 1, 2011, pp. 29–39.
- ¹⁴Menter, F. R., “Two-Equation Eddy-Viscosity Turbulence Models for Engineering Applications,” *AIAA J.*, Vol. 32, No. 8, 1994, pp. 1598–1605.
- ¹⁵Spalart, P. R., and Rumsey, C., “Effective Inflow Conditions for Turbulence Models in Aerodynamic Calculations,” *AIAA J.*, Vol. 45, No. 10, 2007, pp. 2544–2553.
- ¹⁶Sharov, D., and Nakahashi, K. “Reordering of Hybrid Unstructured Grids for Lower-Upper Symmetric Gauss-Seidel Computations,” *AIAA J.*, Vol. 36, No. 3, 1998, pp. 484–486.
- ¹⁷WIND-US User’s Guide, TURBOSPEC - MIT actuator duct (block), <http://www.grc.nasa.gov/WWW/winddocs/user/keywords/turbospec.html> [last updated 21 Apr. 2010; cited 19 Dec. 2012.]
- ¹⁸Defoe, J., “Inlet Swirl Distortion Effects on the Generation and Propagation of Fan Rotor Shock Noise,” Ph.D. Dissertation, Massachusetts Institute of Technology, 2011.
- ¹⁹Hughes, C. E., “Aerodynamic Performance of Scale-Model Turbofan Outlet Guide Vanes Designed for Low Noise,” AIAA–2002–0374, AIAA, 2002. Also NASA/TM—2001-211352, 2011.
- ²⁰Ito, Y., and Nakahashi, K., “Direct Surface Triangulation Using Stereolithography Data,” *AIAA J.*, Vol. 40, No. 3, 2002, pp. 490–496.
- ²¹Ito, Y., Shih, A. M., Soni, B. K., and Nakahashi, K., “Multiple Marching Direction Approach to Generate High Quality Hybrid Meshes,” *AIAA J.*, Vol. 45, No. 1, 2007, pp. 162–167.
- ²²Chima, R. V., “Viscous Three-Dimensional Calculations of Transonic Fan Performance,” *CFD Techniques for Propulsion Applications*, AGARD Conference Proceedings No. CP–510, AGARD, Neuilly sur Seine, France, 1992, pp. 21–1 to 21–19. Also NASA TM–103800, 1992.
- ²³Liou, M.-S., “A sequel to AUSM, Part II: AUSM+–up for all speeds,” *J. Comput. Phys.*, Vol. 214, No. 1, 2006, pp. 137–170.